Materials Science and Engineering B 323 (2026) 118750

Contents lists available at ScienceDirect

Materials Science & Engineering B

journal homepage: www.elsevier.com/locate/mseb

Electrocatalytic Hydrogen and Oxygen Dynamic Production via Magnetic-Field-Induced Aligned Alloyed Nickel-Iron Nanowires

Reza Babashahi [a], Mohammad Mirzaei [a], Reza Rahighi [b], Ali Ghaheri Najafabadi [a], Fatemehsadat Sayyedan [c], Saied Mehran Nahvi [a,*]

[a] Department of Materials Engineering, Isfahan University of Technology, Isfahan 84156-83111, Iran
[b] Institute of Materials Science and Nanotechnology, Bilkent University UNAM, Ankara 06800, Türkiye
[c] Department of Materials Science and Engineering, Faculty of Engineering, Ferdowsi University of Mashhad, Mashhad 9177948944, Iran

ARTICLE INFO

Keywords:
OER Electrocatalyst
Water splitting
Nickel–Iron FeNi NW
Magnetic Field-Assisted Synthesis
Oxygen Evolution Reaction (OER)
Scalable Nanostructure Engineering

ABSTRACT

Optimizing Nickel–iron nanostructure over large surface areas is critical. This study fabricates well-aligned Ni–Fe nanowires on nickel foam, aiming to improve catalytic activity, charge transport, and durability. Using two ferrite permanent magnets during chemical bath deposition, the approach yielded uniform NWs (55–64 nm) compared to disordered morphologies (150–180 nm) formed without magnetic guidance. Characterization via field-emission scanning electron microscopy (FESEM), transmission electron microscopy (TEM), and electrochemical impedance spectroscopy (EIS) confirmed improved nanostructure alignment and reduced charge transfer resistance from 20 Ω to 5.2 Ω. Electrochemical performance tests depicted an overpotential of 230 mV 1.46 V vs. the reversible hydrogen electrode (RHE) at 10 mA/cm^2 and a Tafel slope of 54 mV.dec^{-1}, indicating efficient Oxygen Evolution Reaction (OER) kinetics. The electrochemically active surface area increased to 300 cm^2, which was over 7.5 times greater than that of the substrate (by 40 cm^2), enhancing reaction interfaces. Durability was validated by a minimal 3 mV change over 12 h at 0.5 A/cm^2 and a negligible 0.01 V shift in step-potential tests.

1. Introduction

Hydrogen has emerged as a pivotal clean energy vector in the global pursuit of decarbonization, driven by the urgent need to reduce CO_2 emissions and transition to sustainable energy systems [1–3]. Electrochemical water splitting, in particular, offers an environmentally friendly and scalable approach to hydrogen production [4]. Yet, large-scale deployment faces persistent challenges, including system efficiency, durability of catalytic components, and the economic feasibility of electrode fabrication [5–7]. As advancements in material science and electrochemical engineering converge, water electrolysis is increasingly regarded as a cornerstone of future low-carbon energy infrastructures. The oxygen evolution reaction (OER) is pivotal to the water-splitting process, serving as a kinetic bottleneck due to its sluggish multi-electron transfer mechanisms that impede overall efficiency. Transition metal-based compounds especially first-row transition metals and metal-free carbon materials have shown considerable promise for OER and the hydrogen evolution reaction (HER) [8,9]. Nickel–iron (NiFe) based catalysts in alkaline media have attracted significant interest due to their affordability and exceptional catalytic performance [10]. Notably, the $Ni(OH)_2$ /NiOOH matrix serves as an effective host for Fe incorporation, significantly enhancing OER activity through synergistic effects. NiFe-based catalysts suffer from structural degradation and iron segregation under continuous OER operation, leading to performance decline over time [10].

Various strategies have been proposed to enhance catalytic stability and activity, including the engineering of amorphous structures and metastable phases [11], and heteroatom doping [12] can optimize active site configurations. Moreover, the development of dual-metal single atoms [13] and specific nanostructures [14] can increase active site abundance and facillate mass transport [15,16]. Addressing stability issues and optimizing catalyst design are crucial for the large-scale commercialization of alkaline water electrolysis [10]. Recent studies have explored the use of magnetic fields to enhance the synthesis and performance of OER catalysts [17]. The magnetic-field-assisted chemical corrosion method has been developed to produce $Ni(Fe)(OH)_2$

* Corresponding author.
E-mail address: mehran.nahvi@iut.ac.ir (S.M. Nahvi).

https://doi.org/10.1016/j.mseb.2025.118750
Received 13 July 2025; Received in revised form 24 August 2025; Accepted 28 August 2025
Available online 8 September 2025

-Fe_2O_3 electrodes, achieving an overpotential reduction of 64 mV compared to electrodes synthesized without a magnetic field [17]. Similarly, synthesized MIL-53(Fe–Ni)/NF-2200Gs under an external magnetic field, resulting in superior OER activity with an overpotential of 174 mV at 10 $mA.cm^{-2}$ [18]. A magnetic-field-guided co-electrodeposition strategy has been employed to fabricate Ni–S–$CoFe_2O_4$ nanosheets, achieving an overpotential of 228 mV at 10 $mA.cm^{-2}$ [19]. These investigations illustrate that magnetic fields can promote directional growth, diminish accumulation, increase surface free energy, and alter the chemical state of catalysts, leading to improved OER performance. This approach offers a promising strategy for developing efficient and stable electrocatalysts for sustainable energy applications. These studies highlight the potential of magnetic field-assisted techniques in developing efficient, non-noble metal OER catalysts for water electrolysis [20]. Magnetic field-assisted coating approaches have significant advantages yet encounter numerous restrictions. While magnetic fields can enhance particle incorporation in coatings and improve coating efficiency [20,21], the cost of magnetic field-generating equipment remains a significant barrier to commercial adoption [22]. The dimensions of coated samples are often limited, with many studies conducted in narrow channels or electromagnet bores [20,21]. Methods for generating magnetic fields are varied, including direct current wires [21] and permanent magnets [23]. The intensity and orientation of the magnetic field significantly impact coating outcomes [20,21,24].

This study introduces an innovative magnetic field-assisted chemical bath deposition technique for the large-scale fabrication of NiFe-based electrocatalysts utilizing permanent magnets with an intensity of 110 mT. This technique facilitates the formation of worm-like NWs with high surface area and directional growth, leading to enhanced OER performance. The as-fabricated electrodes aim to provide a practical, low-cost, and scalable solution for integration into water-splitting devices and high-performance alkaline electrolysis systems.

2. Experiments

2.1. Materials

All reagents were used as received without further purification. Iron (III) chloride hexahydrate ($FeCl_3{\cdot}6H_2O$, 99 %), nickel(II) nitrate hexahydrate ($Ni(NO_3)_2{\cdot}6H_2O$, 99 %), sodium citrate dihydrate ($C_6H_5Na_3O_7{\cdot}2H_2O$, ≥99 %), polyvinylpyrrolidone (PVP), potassium hydroxide (KOH, ≥85 %), sodium borohydride ($NaBH_4$, ≥98 %), and hydrazine monohydrate ($N_2H_4{\cdot}H_2O$, 80 %) were purchased from Merck company (Germany). Commercial nickel foam (thickness 1.6 mm, porosity 95 %, Alfa Aesar) was used as the substrate for catalyst deposition.

2.2. Materials Preparation

Nickel foam samples (1 × 1 cm^2) were cleaned prior to use to eliminate surface contaminants and oxides. First, the substrates were immersed in 98 % acetone and sonicated for 5 min in an ultrasonic bath (Elmasonic S30H, Elma, Germany) to remove organic residues. Subsequently, the foams were immersed in 2.0 M hydrochloric acid (HCl) at room temperature (25 °C) for 10 min to eliminate surface oxides. After acid treatment, samples were rinsed thoroughly with double distilled water and ethanol, and dried in a vacuum oven at 70 °C for 1 h.

2.3. Synthesis of Ni foam/NiFe

This work synthesized two fabrication samples: one utilizing a magnetic field (SWMF) and the other without a magnetic field (SWOMF). The magnetic bath utilized for the generation of the SWMF sample was developed. The magnetic bath was made of AISI 304L stainless steel, with two parallel permanent rectangular magnets placed on its sides (**Fig. S1**).

Based on predetermined proportions, 180 mL of dionized water were mixed with $FeCl_3.6H_2O$(16.5 Mm) and then $Ni(NO_3)_2.6H_2O$(33.5 Mm). 37.5 mM of $C_6H_5Na_3O_7.2H_2O$ was added to above solution. 1gr PVP was added to the resultant solution and the pH of the mixture was raised to 13 by adding KOH. Hydrazine monohydrate, 8.5 % by volume and 10 mM sodium borohydride were gradually added to the solution while it was in an electroplating cell in a magnetic field with a strength of 110mT. The temperature of the solution was kept at 80 °C for 1 h.

2.4. Characterization

Comprehensive characterization was conducted to examine the elemental composition, morphology, and structural properties of the synthesized electrocatalyst. X-ray diffraction (XRD) analysis was performed using a Bruker D8 Advance diffractometer equipped with Cu Kα radiation source (λ = 1.5406 Å) over a 2θ range of 10°–80°, at a scanning rate of $0.02^{\circ}{\cdot}s^{-1}$. Field-emission scanning electron microscopy (FESEM) was carried out using a Quanta FEG450 (FEI), and energy-dispersive X-ray spectroscopy elemental mapping was performed via energy dispersive X-ray spectroscopy (EDS) with an EDAX detector**(**EDAX Inc., USA). Transmission electron microscopy (TEM) was conducted using a ZEISS AB LE0912 operating at 100 kV. Wettability was assessed via static water contact angle measurement using a contact angle goniometer equipped with an inverted Canon camera and a micro-syringe (Krüss DSA100, Germany). All measurements were repeated three times at different locations on the sample surface to ensure statistical consistency.

2.5. Electrochemical analysis

All electrochemical measurements were conducted using a three-electrode configuration connected to a potentiostat (EVIUM X.Re, EVIUM Technologies Netherlands,). The prepared Ni foam/NiFe electrode (1 cm^2) served as the working electrode, a platinum wire as the counter electrode, and Ag/AgCl (3 M KCl) as the reference electrode. All potentials were converted to the reversible hydrogen electrode (RHE) using the following equation:

$$E(RHE) = E(Ag/AgCl) + (0.059 \times pH) + 0.197 \quad (1)$$

Electrochemical tests were carried out in 1.0 M KOH aqueous solution (pH ≈ 13.8) at 25 °C. Linear sweep voltammetry (LSV) was performed in the range of 1.2–2.0 V vs. RHE for the oxygen evolution reaction (OER) and from –1.0 to 0 V vs. RHE for the hydrogen evolution reaction (HER) at a scan rate of 5 $mV.s^{-1}$. Electrochemical stability was assessed via chronopotentiometry at a constant current density of 500 mA/cm^2 for 12 h.

To determine the electrochemically active surface area (ECSA), cyclic voltammetry (CV) was conducted in the non-faradaic region (1.0–1.1 V vs. RHE) at various scan rates (20–100 $mV.s^{-1}$), and double-layer capacitance (C_{dl}) was calculated accordingly.

3. Result and discussion

3.1. Materials characterization

In order to identify the phase composition of the nickel–iron coating deposited on the nickel foam substrate, their XRD spectrum was examined. Pure nickel foam exhibited three distinct peaks at 44.5°, 51.9°, and 76.4°, corresponding to the Miller indices (111), (200), and (220), respectively, indicating that nickel possesses a cubic face-centered cubic (FCC) structure (JCPDS No. 04–0850). In the recorded diffraction patterns in Fig. 1, the Ni-Fe NW samples synthesized without and with a magnetic field exhibited diffraction peaks similar to pure nickel, with slight shifts towards lower diffraction angles, and no clear peaks of pure iron or the formation of metallic oxide and hydroxide phases were

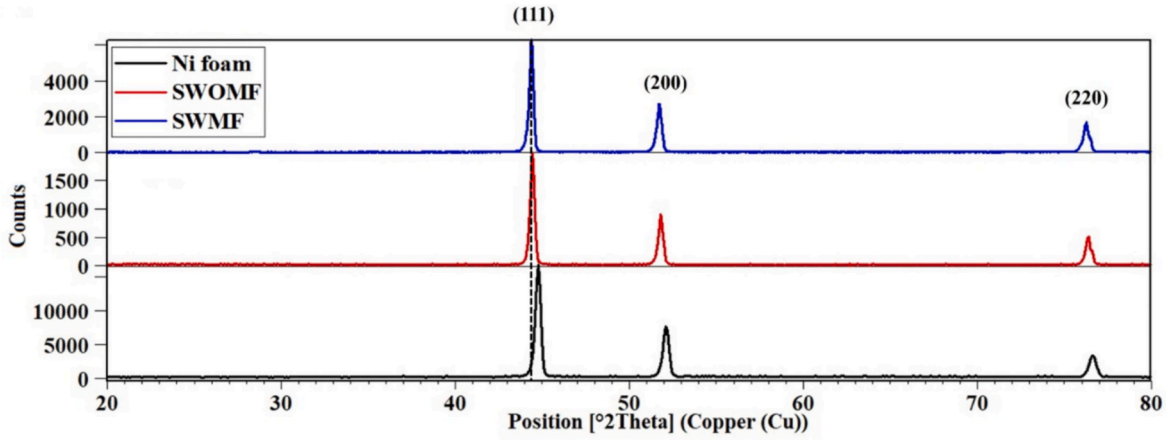

Fig. 1. XRD pattern of Ni foam, NiFe @NF synthesized without magnetic field & NiFe @NF synthesized with magnetic field.

observed. Furthermore, the presence of an increased iron element results in a shift of the (111) plane from 22.26° to 22.2° and 22.1° for the SWOMF and SWMF samples, respectively, while the computed average lattice parameter rises from 3.52 Å to 3.53 Å and 3.54 Å, correspondingly. This could be ascribed to lattice expansion resulting from site-to-site lattice distortions induced by the substitution of Ni atoms with Fe. Furthermore, the diffraction peaks of both synthesized Ni-Fe samples exhibited greater breadth compared to pure nickel, with the peak intensities in the magnetic field-synthesized sample surpassing those in the non-magnetic field-synthesized sample, potentially attributable to lattice distortion and the presence of an amorphous surface peak [25].

FESEM images of the field-free sample in Fig. 2**.a**, exhibit heterogeneous island-like clusters with an average size between 150 to 180 nm, which in Fig. 2**.b** indicate irregular aggregates measuring around 180 nm. The SWMF has a homogeneous, worm-like structure with an average width of 44.4 nm, as seen in Fig. 2**c**. The TEM investigation in Fig. 2**.d** illustrates aligned NWs measuring 55–64 nm in width. Minor variations in width, likely attributable to differences between surface and internal scale measurements, and the absence of ring-like structures in TEM possibly due to sample orientation underscore the magnetic field's pivotal role in orchestrating controlled nanostructure formation. Specifically, the applied magnetic field (110 mT) induces Lorentz forces that enhance ion transport and regulate the directional movement of $Ni2^{+}$ and $Fe3^{+}$ ions toward the nickel foam substrate, promoting uniform nucleation and anisotropic growth of worm-like nanowires. The magnetohydrodynamic effect further induces micro-convective flows in the electrolyte, reducing aggregation and facilitating the formation of aligned nanostructures with reduced diameters (55–64 nm vs. 150–180 nm for SWOMF). This is supported by references to prior studies on magnetic field effects in electrodeposition [19,20], strengthening the scientific grounding of our findings and clarifying the mechanism behind the observed morphological improvements.

Fig. S2 demonstrates the scalability of the magnetic-assisted bath design. A uniform NiFe alloy nanowire coating was successfully deposited on 10 × 10 cm nickel foam substrate. The macroscopic image confirms large-area coverage, while the FESEM insets reveal

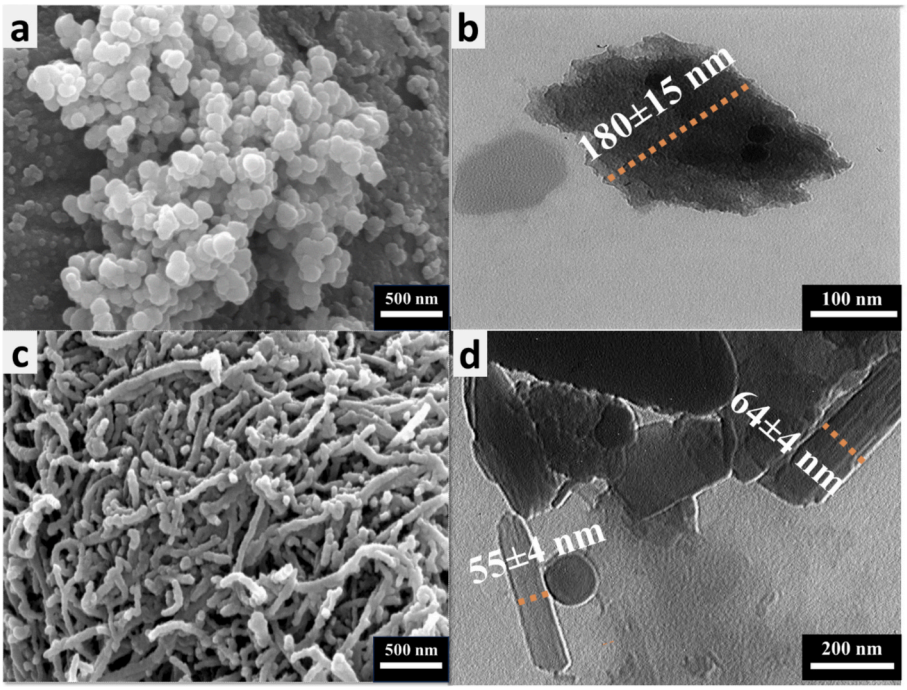

Fig. 2. **(a)**FESEM image of heterogeneous island-like clusters and **(b)** TEM of image of a representative aggregate NiFe @NF synthesized without magnetic field, **(c)** FESEM and **(d)** TEM of NiFe @NF synthesized with magnetic field. EDX-mapping images.

homogeneous nanowire growth across different regions of the electrode. These results support the feasibility of extending the deposition method to larger electrodes with uniform morphology.

The bubbles that grow on the electrode's surface significantly obstruct the active area of the electrode, consequently diminishing the effectiveness of the electrolysis current. Consequently, hydrophilic surfaces facilitate the separation of bubbles from the electrode surface, hence accelerating the kinetics of the reduction reaction. Therefore, enhanced surface hydrophilicity and aerophobicity are highly beneficial, as they facilitate faster electrolyte penetration and easier detachment of gas bubbles, which ultimately promote both OER and HER performance. Due to the non-wettability of pure nickel foam, gas bubbles attach to the foam surface during the water splitting process, evidenced by the computed wettability angle of 83.2 degrees in Fig. 3**a** which indicates the hydrophobic nature of the substrate. The SWOMF sample showed a wettability angle of 29.3 degrees (Fig. 3**b**), indicating lower hydrophilicity compared to the SWMF sample in Fig. 3**c**, which has a wettability angle of 2.8 degrees nearly hydrophilic (approaching zero), allowing gas bubbles to detach from the surface easily in agreement with previous reports that highlight the positive role of hydrophilicity and aerophobicity in enhancing gas-evolution electrocatalysis [26]. Based on the solid–liquid-gas contact theory, micro and nano rough structures can reduce the contact area between bubbles and the electrode [27], which in turn leads to low bubble adhesion and facilitates wetting towards the electrolyte. The high adhesion of the nanocatalyst, which grows directly on the conductive substrate, and the increase in the number of active sites can be considered as two main factors that contribute to this phenomenon.

Fig. S3 provides direct visualization of bubble evolution during electrolysis. On the NiFe alloy nanowire electrode, gas bubbles detach rapidly from the surface, in contrast to the bare Ni foam where bubbles adhere for longer periods. This observation confirms that the enhanced hydrophilicity and aerophobicity of the coated electrode facilitate efficient bubble release, which in turn accelerates mass transport and improves OER/HER kinetics, consistent with the reduced Tafel slope values.

3.2. Electrocatalytic performance

For the purpose of analyzing the electrochemical properties of the coated samples and the substrate, a linear sweep voltammetry (LSV) test was carried out. The LSV curves in OER, as illustrated in Fig. 4**a**, indicate a reduction in overpotential by 2.15 mV 150 mV(from 140 to 300 mV) (from 380 to 230 mV) when comparing pure nickel foam to the nickel–iron composite for achieving a specified current on the surface of the nickel foam. This indicates that by forming a distinct structure, the Ni-Fe combination coating applied with a field has a much higher electrocatalytic activity than the sample produced without a field (overpotential 210 310 mV). The SWMF sample revealed a current density of 10 $mA.cm^{-2}$ at a water splitting potential of 1.46 V, which was obtained to be 1.54 V for the SWOMF sample and 1.61 V for the nickel foam. The overpotential decreases and the reaction rated increases as the recorded value approaches 1.23 V. This pattern was continued. and the sample treated with the magnetic field performed more efficiently due to its NW- and coil-like structure. These structures improve electron transfer due to their high aspect ratio and guiding paths, providing the capability for rapid electron transfer [28,29].

All three samples were subjected to the linear sweep voltammetry test in the HER section (Fig. 4**b**). The catalyst exhibited enhanced performance with increased current density and a closer proximity of the onset potential of the hydrogen reduction current to 0 RHE. The samples SWOMF, SWMF, and nickel foam exhibited optimal performance with onset potentials at current densities of −10 $mA.cm^{-2}$, −0.22, −0.31, and −0.48 V, and current densities of −112, −48, and −12 ($mA.cm^{-2}$) at −0.5 V, respectively.

The EIS test was performed to examine the electrocatalytic interactions between the electrode and electrolyte, as well as to enhance the comprehension of the kinetics of the HER and OER. The charge transfer behavior was assessed by comparing the semicircle diameter in the Nyquist plots using the analogous circuit depicted in Fig. 4**c**. The analogous circuit comprises a solution resistance (R_s), a constant phase element (CPE), and a charge transfer resistance (R_{ct}). Based on these findings, the minimal charge transfer resistance of 5.2 Ω was associated with SWMF, succeeded by SWOMF at 11.8 Ω, while nickel foam exhibited the highest charge transfer resistance at 20 Ω. The SWMF sample, with lower R_{ct} compared to the other samples, indicated a faster catalytic reaction kinetics and an extremely high charge transfer rate in the electrolyte, leading to a reduction in R_{ct} and superior HER catalytic activity, which is consistent with the LSV analysis. The R_s for the samples was found to be 1.3 Ω. A crucial characteristic in evaluating an electrocatalyst is the reaction kinetics, determined by the slope of the tangent line on the potential versus logarithm of current density graph, as derived from **Eq.2**.

$$\eta = b\log j + \alpha \tag{2}$$

Where, j is the current density and b is the Tafel slope, based on the tangent slope obtained from graph in Fig. 4**d**. In general, the lower the Tafel slope of the electrocatalyst, the faster the OER reaction kinetics and the more rapidly the O_2 production rate increases[30]. Nickel foam showed the highest Tafel slope at 143 $mV.dec^{-1}$, while SWOMF had a Tafel slope of 64 $mV.dec^{-1}$ on the high tafel slope scale (60–120 mV/ dec^{-1}): The rate-limitting step is the formation of O* or the release of O_2 [31,32]. The SWMF owned the lowest Tafel slope at 54 $mV.dec^{-1}$ on the moderate tafel slope scale (40–60 mV/ dec^{-1}): The rate-limitting step is the formation of OOH* (O-O bond formation) [30,33]. The high catalytic activity of iron accelerates mass transfer and ion diffusion and improves the rapid release of gas bubbles from the surface of the electrocatalyst. This is beneficial for sufficient contact between the materials and the electrolyte and the adsorption of reactants. The Ni-Fe composition of the SWMF NW sample can effectively regulate the electronic structure and accelerate the kinetics of the catalyst. Results of the wettability test were confirmed by the Tafel test results. Actually, improvements in the Tafel slope a gauge of the effectiveness of electrochemical reactions have a direct correlation with the hydrophilicity of

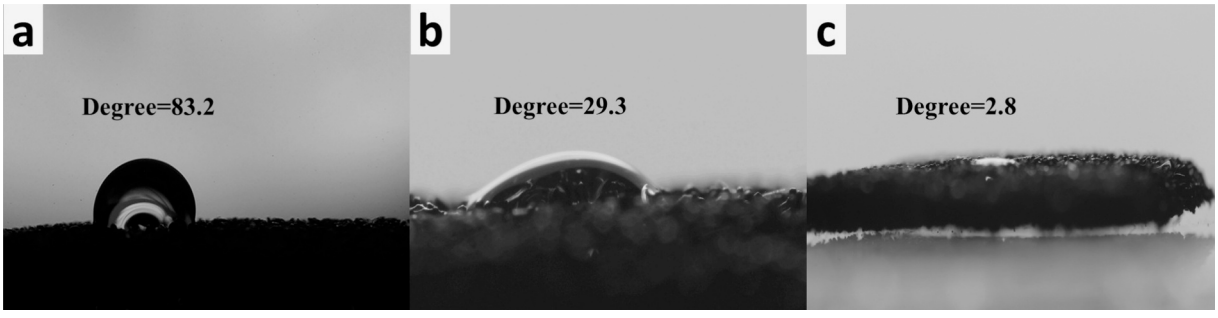

Fig. 3. Digital photos demonstrating wettability testing, **(a)** Ni foam, **(b)** NiFe (SWOMF) **(c)** NiFe(SWMF) After the test.

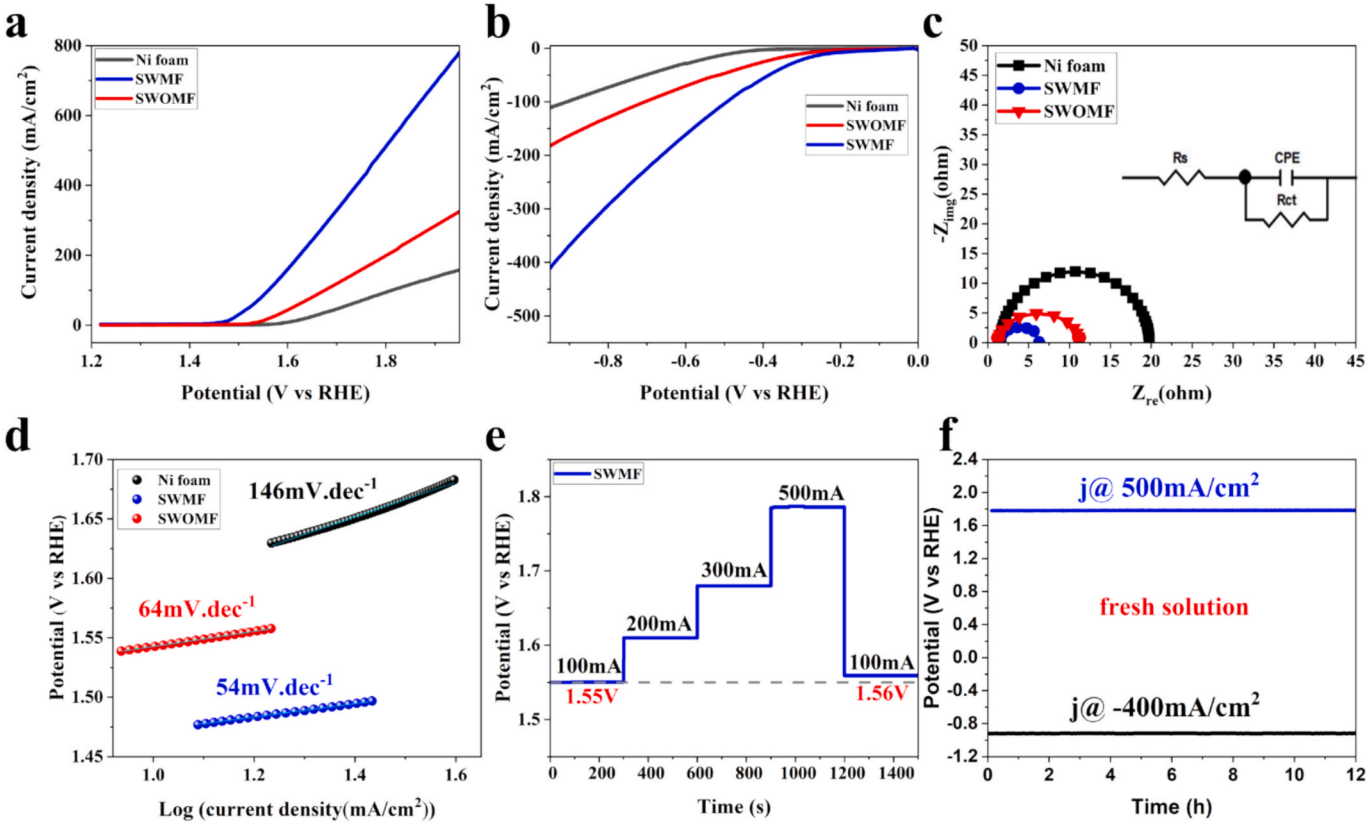

Fig. 4. Electrochemical performance of the as-prepared electrodes for Oxygen and hydrogen evolution catalyses in 1.0 M KOH **(a)** OER polarization curves of Ni foam, NiFe(SWMF), NiFe(SWOMF);**(b)** HER polarization curves of Ni foam, NiFe(SWMF), NiFe(SWOMF);**(c)** EIS Nyquist plots of the **(d)** corresponding Tafel plots, **(e)** step chronoamperometry,**(f)** long term chronoamperometry.

the catalysts. This connection emphasizes how crucial the catalyst's surface characteristics are to maximizing reaction kinetics. Improved Tafel slopes and effective gas evolution are clear indicators that improved mass transfer improves catalytic reaction performance [34,35]. The bifunctional Ni-Fe catalyst developed in this study, in addition to its outstanding performance in the OER, exhibits notable activity in the HER. The application of magnetic field-assisted coating significantly enhanced the HER performance, resulting in a reduction of approximately 90 mV in overpotential at 10 $mA.cm^{-2}$ compared to catalysts prepared without a magnetic field (**Fig. S4**). This improvement is primarily attributed to the optimization of surface morphology and the increased density of catalytic active sites, facilitated by a more uniform distribution of Ni-Fe particles under the influence of the magnetic field. Preliminary mechanistic analysis suggests that the magnetic field likely reduces the activation energy for H^+ adsorption and H* intermediate formation by tuning the electronic structure of the catalyst surface, consistent with recent studies on Ni-Fe-based catalysts [36,37].

Conducting stability testing is one of the most critical evaluations of electrocatalysts. It denotes the projected lifespan and the degree of alterations in the coating and its durability on the surface following electrochemical assessments. Consequently, stepwise chronopotentiometry and long-term chronopotentiometry tests were conducted. In the step chronoamperometry test, as shown in Fig. 4**e**, the initial potential variations were found to be negligible, measuring less than100 mV. The potential variations in the chronoamperometry test, approximately 3 mV as illustrated in Fig. 4**f**, were measured after 12 h at a current density of 500 $mA.cm^{-2}$. The present Ni-Fe NW structure, with approximately 33 % iron and appropriate dispersion (based on EDS tests Fig. 2**e-f**), was resulted in better stability and performance [28,38,39]. These findings underscore the potential of the catalyst as an efficient bifunctional material for electrochemical applications, as observed in the stability of optimized electode as hydrogen evalution catalyst (Fig. 4**f**) and highlight the critical role of the magnetic field-assisted coating method in enhancing HER performance.

An increased number of active sites on the surface enhances the effectiveness of the OER and HER reactions, hence improving the electrochemical performance of the electrocatalyst and subsequently increasing gas generation per unit area of the electrocatalyst. This parameter is directly proportional to the electrochemical surface area (ECSA). The average current density of the output derived from the CV test was determined from Fig. 5 at scan rates ranging from 20 to 100 mVs^{-1}. The current density graphs as a function of the sweep rate were obtained from the average current densities. The SWMF sample, with a slope of 12 mF, possesses the most electrochemically active surface area. ECSA was calculated by dividing the slope of the curve, representing the double-layer capacitance (C_{DL}), by the specific capacitance (C_s). The capacitance value of C_S was obtained to be 40 $\mu F.cm^{-2}$ and has been designated as a standard value in several prior publications [40,41]. Therefore, the active surface plays an important role in the activity of the electrocatalyst. The electrochemically active surface area of the nickel foam was obtained to be 40 cm^2. The SWOMF and SWMF were obtained to be 120 cm^2 and 300 cm^2, respectively. By creating a NW structure, the number of electrochemically active sites was significantly increased. In comparison, the optimal sample with coated samples using a similar method and a higher magnetic field intensity has a calculated slope of 7.94 $mFcm^{-2}$ for Ni-Co-P/NF(600mT) [42] and 3.69 $mF.cm^2$ for Ni(Fe)(OH)2–FeS(MF) [43], indicating better performance due to the improved design of our bath.

Table 1 offered a comparison of OER catalysts, wherein the onset voltage of the reaction at 10 $mA.cm^{-2}$ served as an indicator of thermodynamic activity, while the electrochemical surface area (ECSA) denoted the kinetic activity of the catalyst. The synthesized catalyst has

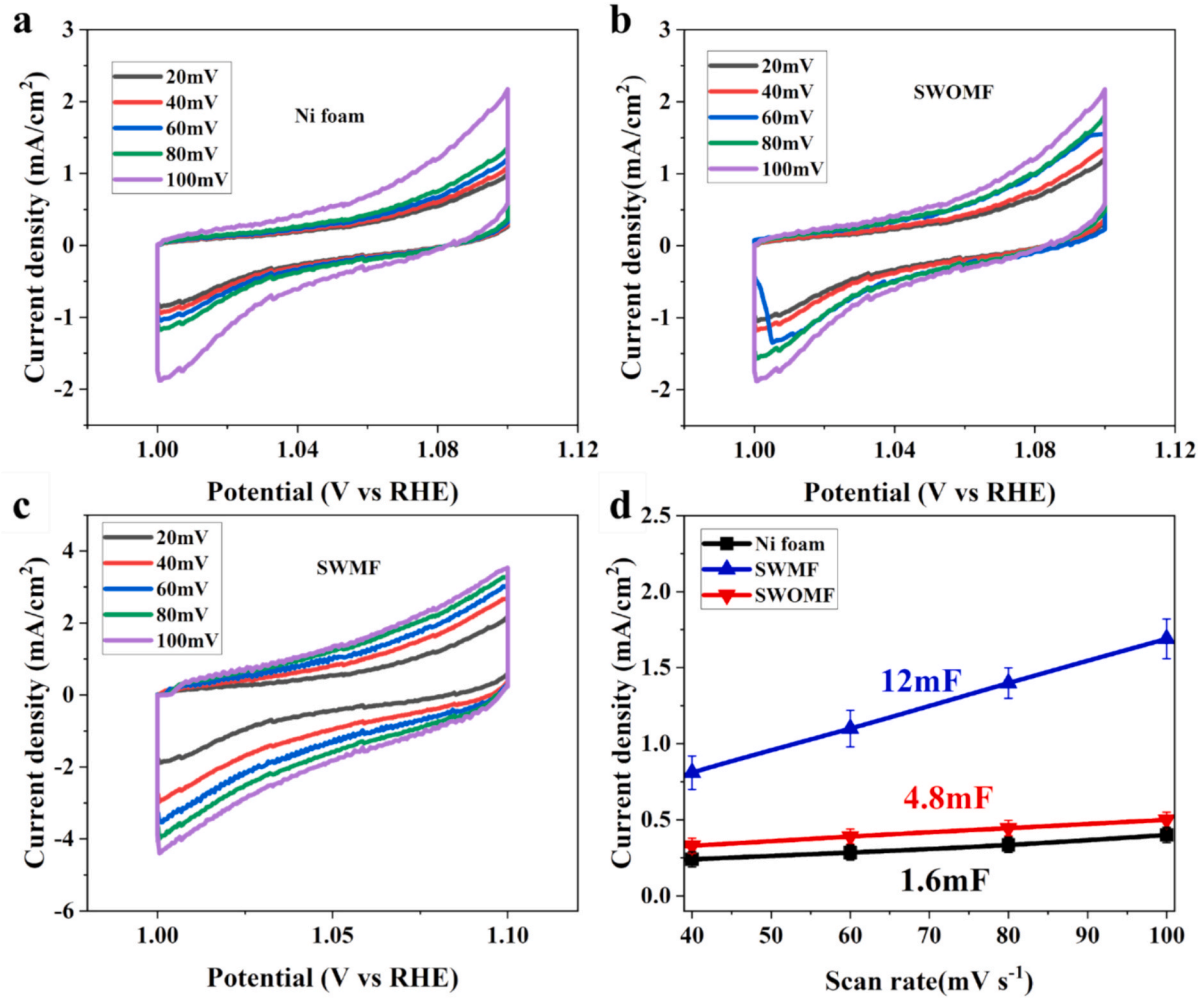

Fig. 5. CV curves measured at different scan rates from 20 to 100 mV of **(a)** Ni foam, **(b)** CVs SWOMF **(c)** CVs SWMF, **(d)** corresponding capacitive current scan rate plots.

Table 1
Summary of various electrocatalysts for water splitting.

Catalyst	Electrolyte	Water splitting voltage (V) at 10 mA.cm^{-2}	ECSA	Reference
NiFe	1MKOH	1.46	12mF cm^{-2*}	This work
W-doped Ni −Fe- P	1MKOH	1.56	Not Reported	[44]
FeCoNiMnMoP	1MKOH	1.49	Not Reported	[45]
Ni-Co-P	1MKOH	1.59	7.94 mF cm^{-2*}	[46]
(Ni, Zn) Fe_2O_4	1MKOH	1.6	Not Reported	[47]
Ni/Fe_3O_4	1MKOH	1.49	11.52mF cm^{-2*}	[48]
NiFe LDH	1MKOH	1.48	3.6 mF cm^{-2*}	[49]

* $C_s = 40\ \mu F/cm^2$.

exhibited activity that aligned more closely with thermodynamic equilibrium conditions and has established an appropriate specific surface area for facilitating kinetic processes.

4. Conclusion

In this work, a novel magnetic bath utilizing permanent magnets with a field strength of 110 mT was developed to prepare NiFe-based electrocatalysts exhibiting a worm-like NW morphology. Compared to the sample synthesized without magnetic assistance, which exhibited an inhomogeneous structure and incomplete coating, the SWMF showed a dense, uniform architecture with a larger electrochemically active surface area, faster electron transfer kinetics, and enhanced superhydrophilicity. The SWMF catalyst demonstrated superior OER performance in 1 M KOH, achieving a lower overpotential of 1.46 V 230 mV at 10 mA.cm^2, a 15.6 % improvement in the Tafel slope, a 2.5-fold increase in electrochemical active surface area, and a 2.26-fold decrease in charge transfer resistance. These enhancements are attributed to improved nonstructural alignment, increased wettability, and more efficient gas bubble release. Moreover, the scalable design of the magnetic bath enables uniform catalyst deposition over larger areas, presenting practical advantages for industrial electrode fabrication. This study demonstrates an effective and scalable strategy for engineering high-performance, non-noble metal OER electrocatalysts, with promising potential for broader applications in electrochemical energy systems.

5. Compliance with Ethical Standards

The data presented in this manuscript have never been published

before and are not currently being reviewed by any other journal. If this article is accepted, it will not be published anywhere else in its current or translated form without the written permission of the Publisher. All authors have agreed that the article is original and have given their approval for its submission.

Research data Policy and data availability Statements

The data presented in this study are available on request from the corresponding author.

CRediT authorship contribution statement

Reza Babashahi: Writing – original draft, Visualization. **Mohammad Mirzaei:** Project administration. **Reza Rahighi:** Investigation, Data curation. **Ali Ghaheri Najafabadi:** Writing – review & editing, Visualization, Investigation. **Fatemehsadat Sayyedan:** Writing – review & editing, Validation, Data curation. **Saied Mehran Nahvi:** Supervision, Investigation.

Declaration of competing interest

The authors declare that they have no known competing financial interests or personal relationships that could have appeared to influence the work reported in this paper.

Appendix A. Supplementary data

Supplementary data to this article can be found online at https://doi.org/10.1016/j.mseb.2025.118750.

Data availability

No data was used for the research described in the article.

References

[1] A.M. Sadeq, et al., Hydrogen energy systems: Technologies, trends, and future prospects, Sci. Total Environ. vol. 939 (2024/08/20/ 2024,) 173622, https://doi.org/10.1016/j.scitotenv.2024.173622.

[2] A. Franco, "Green Hydrogen and the Energy Transition: Hopes, Challenges, and Realistic Opportunities," *Hydrogen,* vol. 6, no. 2, p. 28, 2025. [Online]. Available: https://www.mdpi.com/2673-4141/6/2/28.

[3] I. Elegbeleye, O. Oguntona, and F. Elegbeleye, "Green Hydrogen: Pathway to Net Zero Green House Gas Emission and Global Climate Change Mitigation," *Hydrogen,* vol. 6, no. 2, p. 29, 2025. [Online]. Available: https://www.mdpi.com/2673-4141/6/2/29.

[4] J. Liang, et al., Defect engineering induces Mo-regulated Co9Se8/FeNiSe heterostructures with selenium vacancy for enhanced electrocatalytic overall water splitting in alkaline, J. Colloid Interface Sci. 655 (2024/02/01/ 2024,) 296–306, https://doi.org/10.1016/j.jcis.2023.11.010.

[5] B.S. Zainal, et al., Recent advancement and assessment of green hydrogen production technologies, Renew. Sustain. Energy Rev. vol. 189 (2024/01/01/ 2024,) 113941, https://doi.org/10.1016/j.rser.2023.113941.

[6] I. Marouani, et al., Integration of renewable-energy-based green hydrogen into the energy future, Processes 11 (9) (2023) 2685.

[7] B. Amini Horri, H. Ozcan, Green hydrogen production by water electrolysis: current status and challenges, Curr. Opin. Green Sustainable Chem. vol. 47 (2024/06/01/ 2024,) 100932, https://doi.org/10.1016/j.cogsc.2024.100932.

[8] K. Zhang, R. Zou, Advanced transition Metal-based OER electrocatalysts: current status, opportunities, and challenges, Small 17 (37) (2021/09/01 2021,) 2100129, https://doi.org/10.1002/smll.202100129.

[9] P. Li, et al., Recent advances in the Development of Water Oxidation Electrocatalysts at Mild pH, Small 15 (13) (2019/03/01 2019,) 1805103, https://doi.org/10.1002/smll.201805103.

[10] Y. Han, et al., Stability challenges and opportunities of NiFe-based electrocatalysts for oxygen evolution reaction in alkaline media, Carbon Neutralization 3 (2) (2024/03/01 2024,) 172–198, https://doi.org/10.1002/cnl2.110.

[11] Z. Xue, et al., Interfacial Electronic Structure Modulation of NiTe Nanoarrays with NiS nanodots facilitates electrocatalytic oxygen evolution, Adv. Mater. 31 (2019).

[12] L. Tian, et al., Cation-Anion dual Doping Modifying Electronic Structure of Hollow CoP nanoboxes for enhanced water oxidation electrocatalysis, Inorg. Chem. (2022).

[13] J. Yin, et al., Iridium Single Atoms Coupling with Oxygen vacancies boosts oxygen evolution reaction in acid media, J. Am. Chem. Soc. (2020).

[14] S. Zhao, et al., Gold Nanoclusters promote electrocatalytic water oxidation at the Nanocluster/CoSe2 Interface, J. Am. Chem. Soc. 139 (3) (2017) 1077–1080.

[15] F. Bao, et al., Host, Suppressor, and Promoter—The Roles of Ni and Fe on Oxygen Evolution Reaction activity and Stability of NiFe Alloy Thin Films in Alkaline Media, ACS Catal. 11 (16) (2021/08/20 2021,) 10537–10552, https://doi.org/10.1021/acscatal.1c01190.

[16] Q. Kang, D. Lai, W. Tang, Q. Lu, F. Gao, Intrinsic activity modulation and structural design of NiFe alloy catalysts for an efficient oxygen evolution reaction, Chem. Sci. 12 (11) (2021) 3818–3835.

[17] M. Xu, et al., Construction of Ferric-Oxide-Doped Nickel–Iron Hydroxide Electrocatalysts by Magnetic-Field-Assisted Chemical Corrosion toward Boosted Oxygen Evolution Reaction, Molecules 29 (13) (2024) 3127.

[18] Y. Miao, et al., One-pot synthesis of NiFe nanoarrays under an external magnetic field as an efficient oxygen evolution reaction catalyst, RSC Adv. 13 (7) (2023) 4249–4254.

[19] L. Zhang, J. Peng, Y. Yuan, K. Peng, Magnetic enhancement of oxygen evolution reaction performance of NiCo-spinel oxides, Nanotechnology 32 (50) (2021/10/07 2021,) 505716, https://doi.org/10.1088/1361-6528/ac28d6.

[20] H.A. Murdoch, E. Hernández-Rivera, A. Thornton, D. Yin, A.K. Giri, Magnetic field-enabled co-electrodeposition of luminescent yttria particles, Scr. Mater. 188 (2020/11/01/ 2020,) 212–215, https://doi.org/10.1016/j.scriptamat.2020.07.025.

[21] S. Akar, S. Rashidi, J. Esfahani, N. Karimi, Targeting a channel coating by using magnetic field and magnetic nanofluids, J. Therm. Anal. Calorim. 137 (2019) 381–388.

[22] A.M. Iderawumi, C.E. Friday, Effects of magnetic field on pre-treament of seedlings and germination, Journal of Agriculture and Research 6 (9) (2020) 1–8.

[23] B. Jelenc, Generating Uniform magnetic Fields in 2-D Polygonal Regions, IEEE Trans. Magn. 57 (2021) 1–5.

[24] Y. Zhu, H. Zhou, Z. Chen, Z. Wang, F. He, C. Xu, Study on Microstructure and Properties of Ni60A/WC Composite Coating by Alternating-Magnetic-Field-Assisted Laser Cladding, Micromachines 13 (2022).

[25] C. Liang *et al.*, "Exceptional performance of hierarchical Ni–Fe oxyhydroxide@NiFe alloy nanowire array electrocatalysts for large current density water splitting," *Energy & Environmental Science,* 10.1039/C9EE02388G vol. 13, no. 1, pp. 86–95, 2020, doi: 10.1039/C9EE02388G.

[26] J. Li, et al., Self-supported molybdenum nickel oxide catalytic electrode designed via molecular cluster-mediated electroplating and electrochemical activation for an efficient and durable oxygen evolution reaction, J. Colloid Interface Sci. 628 (2022/12/15/ 2022,) 607–618, https://doi.org/10.1016/j.jcis.2022.08.009.

[27] Y. Xing, et al., Effect of surface roughness on the detachment between bubble and glass beads with different contact angles, Powder Technol. 361 (2020) 812–816.

[28] C. Jing, et al., Efficient electrocatalytic water oxidation by using the hierarchical 1D/2D structural nanohybrid of CoCu-based zeolitic imidazolate framework nanosheets and graphdiyne nanowires, Electrochim. Acta (2020).

[29] W. Wang, et al., Design, synthesis and electrocatalytic properties of coaxial and layer-tunable MoS2 nanofragments/TiO2 nanorod arrays, Chem. Commun. 53 (39) (2017) 5461–5464.

[30] L. Negahdar, F. Zeng, S. Palkovits, C. Broicher, R. Palkovits, Mechanistic aspects of the electrocatalytic oxygen evolution reaction over Ni−Co Oxides, ChemElectroChem (2019).

[31] J. Huang, X. Zhu, M.H. Eikerling, The rate-determining term of electrocatalytic reactions with first-order kinetics, Electrochim. Acta 393 (2021) 139019.

[32] J.O.M. Bockris, Kinetics of Activation Controlled Consecutive Electrochemical Reactions: Anodic Evolution of Oxygen, J. Chem. Phys. 24 (1956) 817–827.

[33] D. Friebel, et al., Identification of Highly active Fe Sites in (Ni,Fe)OOH for Electrocatalytic Water Splitting, J. Am. Chem. Soc. 137 (3) (2015/01/28 2015,) 1305–1313, https://doi.org/10.1021/ja511559d.

[34] E. Kemppainen, J. Halme, O. Hansen, B. Seger, P.D. Lund, Two-phase model of hydrogen transport to optimize nanoparticle catalyst loading for hydrogen evolution reaction, Int. J. Hydrogen Energy 41 (2016) 7568–7581.

[35] C. Zhang, et al., Superaerophilic/superaerophobic cooperative electrode for efficient hydrogen evolution reaction via enhanced mass transfer, Sci. Adv. 9 (2023).

[36] L. Wei, D. meng, Q. Jiang, W. Wang, and J. Tang, "A review on oxygen evolution electrocatalysts based on the different Ni-Fe matrix composites," *Journal of Environmental Chemical Engineering,* vol. 10, no. 6, p. 108591, 2022/12/01/ 2022, doi: https://doi.org/10.1016/j.jece.2022.108591.

[37] T. Xiong, Z. Zhu, Y. He, M.S. Balogun, Y. Huang, Phase evolution on the hydrogen adsorption kinetics of NiFe-based heterogeneous catalysts for efficient water electrolysis, Small Methods 7 (4) (2023) 2201472.

[38] S. Czioska, J. Wang, S. Zuo, X. Teng, Z. Chen, Hierarchically Structured NiFeOx/CuO nanosheets/nanowires as an efficient electrocatalyst for the oxygen evolution reaction, ChemCatChem 10 (2018).

[39] P. Acharya, et al., Chemical Structure of Fe–Ni Nanoparticles for Efficient Oxygen Evolution Reaction Electrocatalysis, ACS Omega 4 (2019) 17209–17222.

[40] H. Fei, et al., Atomic cobalt on nitrogen-doped graphene for hydrogen generation, Nat. Commun. 6 (1) (2015) 1–8.

[41] C.C. McCrory, S. Jung, I.M. Ferrer, S.M. Chatman, J.C. Peters, T.F. Jaramillo, Benchmarking hydrogen evolving reaction and oxygen evolving reaction electrocatalysts for solar water splitting devices, J. Am. Chem. Soc. 137 (13) (2015) 4347–4357.

[42] Z. Wang, et al., Magnetic field assisted synthesis of dense braided rope NiCoP as a highly efficient hydrogen evolution electrocatalyst, Appl Catal B 343 (2024) 123579.

[43] X. Zhang, et al., Magnetic field-assisted microbial corrosion construction iron sulfides incorporated nickel-iron hydroxide towards efficient oxygen evolution,

Chin. J. Struct. Chem. 43 (1) (2024/01/01/ 2024,) 100200, https://doi.org/10.1016/j.cjsc.2023.100200.

[44] K. Xiong, H. Zhao, F. Du, G. Xie, T., Xie, "Facile synthesis of highly active monolithic water-separated W-doped Ni–Fe–P catalysts,", Int. J. Hydrogen Energy 48 (70) (2023/08/15/ 2023,) 27105–27111, https://doi.org/10.1016/j.ijhydene.2023.03.371.

[45] Z. Wang, et al., Sabatier principle based design of high performance FeCoNiMnMoP high entropy electrocatalysis for alkaline water splitting, Chem. Eng. J. 497 (2024/10/01/ 2024,) 154650, https://doi.org/10.1016/j.cej.2024.154650.

[46] J. Chang, et al., Enhanced electrocatalytic efficiencies for water electrolysis and para-nitrophenol hydrogenation by self-supported nickel cobalt phosphide-nickel iron layered double hydroxide p-n junction, J. Colloid Interface Sci. 653 (2024/01/01/ 2024,) 1063–1074, https://doi.org/10.1016/j.jcis.2023.09.156.

[47] M. Xia, et al., Magnetic field induced synthesis of (Ni, Zn)Fe2O4 spinel nanorod for enhanced alkaline hydrogen evolution reaction, Prog. Nat. Sci.: Mater. Int. 33 (2) (2023/04/01/ 2023,) 172–177, https://doi.org/10.1016/j.pnsc.2023.04.001.

[48] F. Zhu, Y. Wang, Y. Chen, M. Wu, W. Jiang, Magnetic field-assisted electrodeposition of Fe3O4 nanoparticles on Ni as bifunctional electrocatalyst for overall water splitting, ACS Appl. Nano Mater. 6 (21) (2023) 19837–19847.

[49] J. Wang *et al.*, "Hierarchical NiFe LDH/N-doped Co/nickel foam as highly active oxygen evolution reaction electrode for anion exchange membrane water electrolysis," *Nano Research,* vol. 18, no. 2, 2025.